

Lunar equatorial surface temperatures and regolith properties from the Diviner Lunar Radiometer Experiment

Ashwin R. Vasavada,¹ Joshua L. Bandfield,² Benjamin T. Greenhagen,¹ Paul O. Hayne,³ Matthew A. Siegler,⁴ Jean-Pierre Williams,⁴ and David A. Paige⁴

Received 30 September 2011; revised 20 February 2012; accepted 20 February 2012; published 4 April 2012.

[1] The Diviner Lunar Radiometer Experiment onboard the Lunar Reconnaissance Orbiter has measured solar reflectance and mid-infrared radiance globally, over four diurnal cycles, at unprecedented spatial and temporal resolution. These data are used to infer the radiative and bulk thermophysical properties of the near-surface regolith layer at all longitudes around the equator. Normal albedos are estimated from solar reflectance measurements. Normal spectral emissivities relative to the 8- μm Christiansen Feature are computed from brightness temperatures and used along with albedos as inputs to a numerical thermal model. Model fits to daytime temperatures require that the albedo increase with solar incidence angle. Measured nighttime cooling is remarkably similar across longitude and major geologic units, consistent with the scarcity of rock exposures and with the widespread presence of a near-surface layer whose physical structure and thermal response are determined by pulverization through micrometeoroid impacts. Nighttime temperatures are best fit using a graded regolith model, with a $\sim 40\%$ increase in bulk density and an eightfold increase in thermal conductivity (adjusted for temperature) occurring within several centimeters of the surface.

Citation: Vasavada, A. R., J. L. Bandfield, B. T. Greenhagen, P. O. Hayne, M. A. Siegler, J.-P. Williams, and D. A. Paige (2012), Lunar equatorial surface temperatures and regolith properties from the Diviner Lunar Radiometer Experiment, *J. Geophys. Res.*, 117, E00H18, doi:10.1029/2011JE003987.

1. Introduction and Background

[2] The Moon experiences extremes in surface temperature due to its slow rotation, lack of atmosphere, and the near-ubiquitous presence of a highly insulating regolith layer. Equatorial daytime temperatures reach 400 K, while nighttime temperatures fall below 100 K. Because the sub-solar point remains within $\sim 1.59^\circ$ of the equator over the lunar year and nodal precession cycle, surfaces at high latitudes experience persistently large solar incidence angles and cold temperatures. Some regions near the poles are permanently obscured from direct illumination by topography and have annual maximum surface temperatures near 30 K, with implications for trapping and retaining water ice and other volatiles [Vasavada *et al.*, 1999; Paige *et al.*, 2010b]. Details of the regolith's thermal response to solar forcing provide information about the radiative and thermophysical properties, structure, and rock abundance of the

near-surface layer. These properties, as well as surface temperature and volatile stability, are of interest both scientifically and for planning lunar robotic and human exploration.

[3] Lunar surface temperatures have been measured for several decades using Earth-based infrared and radio telescopes, instruments aboard lunar orbiters, and in situ experiments at the Surveyor and Apollo sites [see Paige *et al.*, 2010a, and references therein]. Returned samples have helped constrain regolith properties such as albedo, particle size distribution, bulk density, thermal conductivity, and heat capacity. Together these data sets provide a basic understanding of the lunar regolith. A more detailed, contextual understanding requires a data set with systematic and comprehensive geographic, temporal, and spectral (visible and thermal infrared) coverage, high spatial resolution, sensitivity to all lunar temperatures, and correspondingly detailed topographic data. The collection of such data has been a primary goal of the Lunar Reconnaissance Orbiter (LRO) mission [Vondrak *et al.*, 2010]. Its measurements allow, for example, the assessment of spatial variations in regolith properties, the effects of surface roughness and slopes, and the correlations between thermal data and compositional or geological characteristics.

[4] The LRO launched on 18 June 2009 and entered lunar orbit five days later. On 15 September, after a commissioning period, the LRO transitioned to a low-altitude (~ 50 km), circular, polar orbit fixed in inertial space [Tooley *et al.*, 2010]. This orbit was designed to allow repetitive, high

¹Jet Propulsion Laboratory, California Institute of Technology, Pasadena, California, USA.

²Earth and Space Sciences, University of Washington, Seattle, Washington, USA.

³Geological and Planetary Sciences, California Institute of Technology, Pasadena, California, USA.

⁴Earth and Space Sciences, University of California, Los Angeles, California, USA.

spatial resolution coverage of polar latitudes as local time and season (i.e., solar declination) varied over the one-year prime mission. The Diviner Lunar Radiometer Experiment began systematically measuring the visible and thermal radiance from the Moon during the commissioning period and has since operated nearly continuously. The Diviner investigation is unique in the quality of its data, its spatial and temporal coverage, and its high spatial resolution.

[5] This paper describes the contributions of Diviner to understanding the thermophysical properties and structure of the near-surface layer. A companion paper looks specifically at the influence of rocks [Bandfield *et al.*, 2011]. We constrain our analysis to a narrow band around the lunar equator in order to reduce the effects of latitude (i.e., the combined effects of incidence angle, roughness, and topography), while still sampling a swath of terrain that globally represents the lunar surface layer. Throughout the paper, we use east longitude and the following notation:

- A albedo, as defined in the text.
- ϵ_i spectral emissivity of Diviner channel i .
- θ solar incidence angle, degrees.
- k regolith bulk thermal conductivity, W/m/K.
- λ wavelength, μm .
- μ_0 cosine of the solar incidence angle.
- ρ regolith bulk density, kg/m^3 .
- T_i brightness temperature of Diviner channel i , K.
- T_B brightness temperature, K.
- z depth below the surface, m.

2. Diviner Data Set and Its Characteristics

[16] The Diviner experiment is a nadir-pointed, push-broom scanning radiometer with two spectral channels for reflected solar radiation, each 0.35 to 2.8 μm , and seven channels for infrared emission, spanning 7.55 to 400 μm [Paige *et al.*, 2010a]. It is designed to globally map surface albedo and temperature over the lunar diurnal and seasonal cycles, including regions of extremely low temperature at the poles. Three of the infrared channels also assess composition by accurately locating the silicate mid-infrared emissivity peak (Christiansen Feature) near 8 μm [Conel, 1969]. At an orbital altitude of 50 km, Diviner's spatial resolution is approximately 320 m along track, set by signal timing, and 160 m across track, set by the fields of view of the twenty-one detectors in each of nine linear arrays. Nadir data are acquired nearly continuously along a north-south orbit track with an image swath of 3.4 km. Regular interruptions in coverage allow for Diviner space and blackbody calibrations. Irregular interruptions occur when the spacecraft rolls to enable targeted observations by other LRO instruments.

[17] Because LRO's polar orbit is fixed in inertial space, the local time beneath the spacecraft varies slowly over the year until two complete diurnal cycles (one each from the ascending and descending orbit tracks) are captured by Diviner. Each orbit track is aligned north-south and is nearly constant in local time. The Moon also rotates on its axis each month, spreading the local time coverage over all longitudes. Each period of full longitudinal coverage is referred to as one mapping cycle. Diviner's spatial and local time coverage far exceeds what was available before, but certain limitations

are present. Irregular spacing of successive orbit tracks results in duplicate spatial coverage at some longitudes and gaps at others, especially at lower latitudes. The temporal sampling of any particular low-latitude location is typically no better than about every two hours of local time. However, finer temporal resolution can be obtained by using data from a wider swath of longitudes. At polar latitudes the observation pattern is similar, but features of a given physical size receive many more observations than at the equator due to the convergence of orbit tracks.

2.1. Measurement Effects on Diviner Brightness Temperatures

[18] Each Diviner measurement ideally could be converted to a physical surface temperature. However, the scene viewed by each of Diviner's detectors contains a distribution of physical temperatures due to small-scale slopes, shadows, rocks, and spatially variable photometric and thermophysical properties. Diviner measures infrared radiance within seven spectral bands that sample different portions of the emitted thermal radiation. When sub-detector scale anisothermality is present, the derived brightness temperatures in each infrared spectral channel differ from one another. Shorter-wavelength channels have higher brightness temperatures due to the nonlinearity of the Planck function; they are more sensitive to the warmer portions of the scene. The anisothermality effect increases when large illumination or viewing angles enhance the influence of roughness, topography, and shadowing. It can also affect un-illuminated surfaces, e.g., when local variations in thermophysical properties (such as the presence of rocks) result in persistent temperature contrasts at night, as discussed in a companion paper [Bandfield *et al.*, 2011].

[19] In their study of the south polar region, Paige *et al.* [2010b] addressed spectral differences by calculating a bolometric brightness temperature using measured spectral radiances across several channels. In the present study, we use a single channel (T_7 , 25–41 μm) because of its high signal-to-noise over the full range of equatorial surface temperatures. While rare rocky areas can increase nighttime T_7 by tens of Kelvin, most lunar surfaces contain less than 1% rock coverage and the typical rock population has a relatively small (<1 K) influence on T_7 [Bandfield *et al.*, 2011].

2.2. Equatorial Data Set

[20] We created an equatorial data set (EDS) by extracting all Diviner observations between -0.2° and 0.2° latitude that were acquired in nadir mapping mode between 6 July 2009 and 31 August 2011. There are approximately 21 million separate measurements per channel. The data set captures 29 mapping cycles and more than four diurnal cycles (two on each node of Diviner's orbit).

[21] Figure 1 shows how selected orbital parameters vary with time in the EDS. High orbit altitudes prior to 15 September 2009 and the generally elliptical orbit shape result in significant variability in footprint size, but we find no systematic effect on measured brightness temperature. The latitude and longitude of each Diviner footprint are initially calculated on a sphere with no topography. Because the observations are slightly off-nadir due to Diviner's $\sim 4^\circ$ total field of view, lunar topography will affect where a ray traced

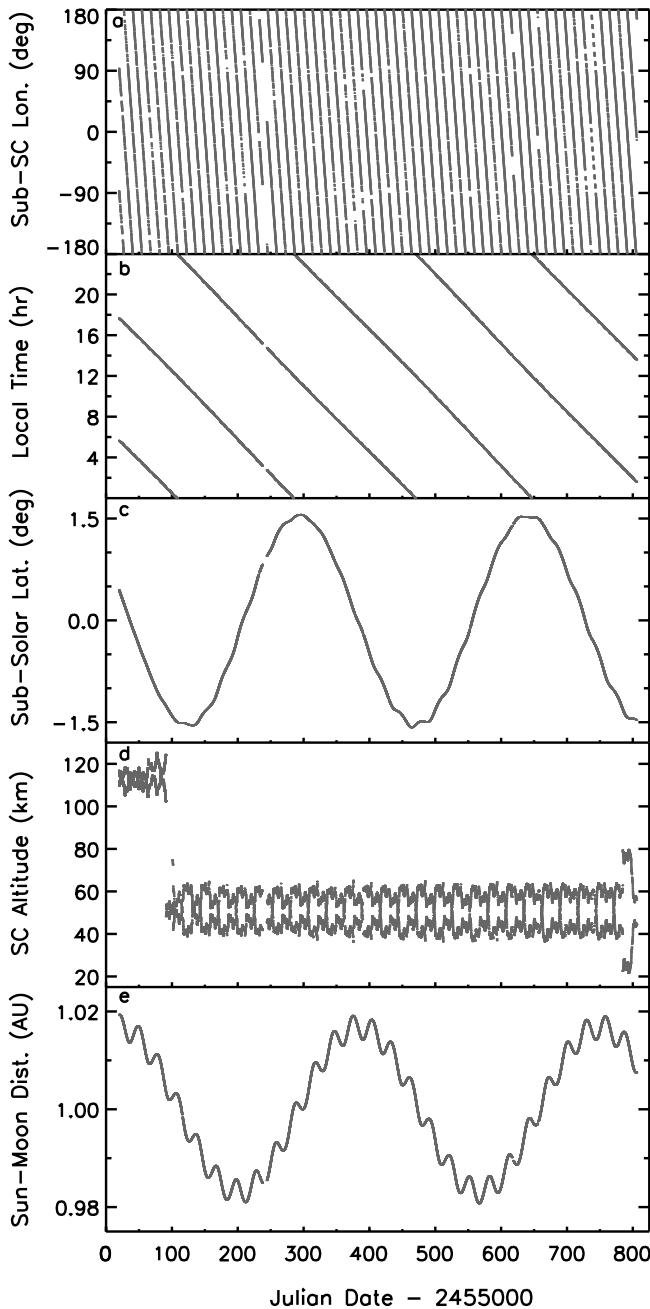


Figure 1. Variations in orbital and celestial parameters within the Equatorial Data Set. Quantities are plotted against Julian Date (2455000 is 17 June 2009). (a and b) The longitude and local solar time at the equator below the spacecraft's two ground tracks (i.e., the ascending and descending nodes of the orbit). (c) The sub-solar latitude, which varied between -1.58° and 1.56° over this time period. (d) The spacecraft's orbital altitude, calculated relative to a spherical moon with a radius of 1737.4 km. The altitude in the early part of the mission varied between 102 and 125 km. The spacecraft then transitioned to a lower orbit with altitude varying between 36 and 67 km, except in the final month. (e) The distance between the centers of the Sun and Moon. Gaps in the data set show up as gaps in the curves.

from the instrument intersects the surface. We use the UCLA Digital Moon topographic model, created by fitting a triangular mesh with a resolution of 0.5 km to the Lunar Orbiter Laser Altimeter (LOLA) data set [Smith *et al.*, 2010], to estimate the local surface slope and refine each footprint's location and orientation [Paige *et al.*, 2010b]. Solar and lunar geometries are derived using ephemerides publicly available from the Navigation and Ancillary Information Facility (NAIF) at the Jet Propulsion Laboratory.

[22] Figures 2a and 2b show local time coverage and slope distribution versus longitude. The temporal coverage at any given longitude is every ~ 2 h and local time and longitude remain correlated in this data set. Mare and highland surfaces clearly differ in their surface slope characteristics, with the former having slopes less than 2° in our digital elevation model (with some exceptions), and the latter having a broad distribution of slopes up to 20° – 30° .

3. Diviner-Derived Albedo and Emissivity

[23] The following sections describe our process for estimating the solar albedo and infrared emissivity of the lunar surface versus longitude at the equator, necessary as inputs to our thermal model. Our estimates of Diviner albedo and emissivity are strictly a means of improving the accuracy when deriving surface thermophysical properties. We intentionally constrain our analyses (e.g., by significantly filtering the input Diviner measurements) to simplify the treatment of spectral and angular effects. A full understanding of lunar photometry and emission from Diviner awaits future studies. The error associated with these methods is described in section 6.

3.1. Albedo

[24] The albedo of the lunar surface can be derived from Diviner's broadband solar channels. Channels 1 and 2 both measure scattered sunlight between 0.3 and $3\ \mu\text{m}$, but channel 2 has a neutral density filter that reduces its sensitivity [Paige *et al.*, 2010a]. Here we use calculated values of relative surface reflectance (a Diviner data product archived in the Planetary Data System) derived from channel 1. It is the ratio of the radiance from the lunar surface to that of a perfectly reflective, normally illuminated, Lambert surface at the location of the spacecraft.

[25] The measured relative reflectance has an opposition surge at low phase angles, then decreases with increasing solar phase angle (primarily due to illumination, not to be confused with any angular dependence of albedo). To exclude the surge and reduce scatter from topographic effects, we restrict local time to 8–10 and 14–16 h (i.e., incidence angles of 30° – 60° and equivalent phase angles given the nadir observational geometry) and remove points with a local slope $>2^\circ$. Within this constrained data set, we find that for darker surfaces, the dependence of reflectance on phase angle can be removed by dividing by $\mu_0^{1.3}$. This is a slightly stronger dependence than for a Lambertian surface (i.e., dividing by μ_0). It is difficult to assess its appropriateness for brighter surfaces due to (unresolved) surface slopes that cause higher levels of scatter in the data.

[26] We use the derived dependence to remove the illumination effect from all data points. We take the resulting quantity (the reflectance of the lunar surface at zero phase

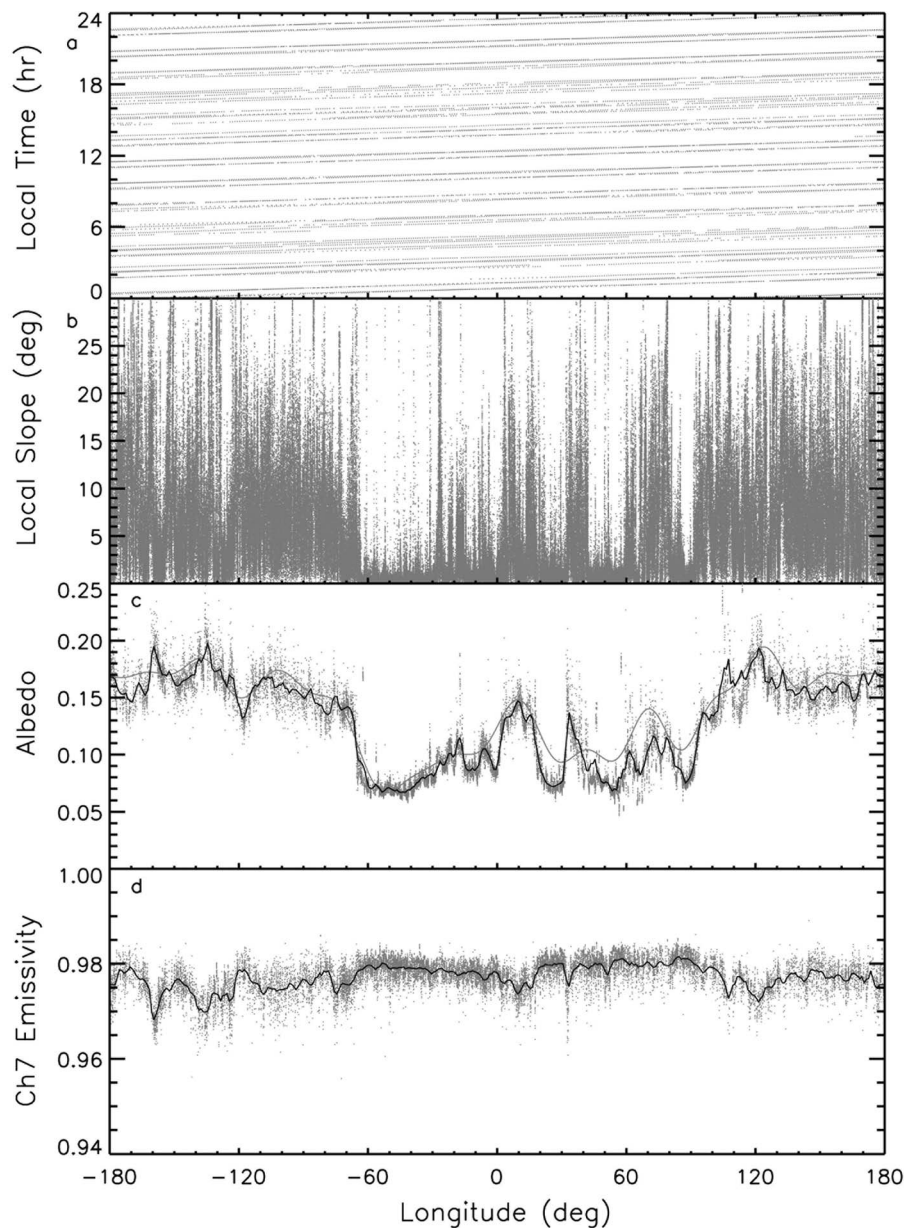


Figure 2. Local time coverage, local slope distribution, albedo, and spectral emissivity from the equatorial data set. (a) Local time of each Diviner data point. (b) The angular difference between the normal vector of a non-sloped surface and the local normal vector of each Diviner point taken from the UCLA Digital Moon mesh. The data are truncated at 30° . (c) Average Diviner albedo in each $0.05^\circ \times 0.05^\circ$ bin (points), the profile smoothed as described in the text (black line), and the DLAM-1 model (gray line). (d) Channel 7 spectral emissivity averaged in each bin and its smoothed profile (black line).

angle with the opposition surge removed) to represent the fraction of insolation that is not absorbed, hereafter called normal albedo, or albedo. Figure 2c includes a profile of normal albedo versus longitude, smoothed by a moving average of all data within 2° of longitude, every 0.05° of longitude.

[27] Mean albedos for mare and highland surfaces are approximately 0.07 and 0.16, respectively. In Figure 2c we compare Diviner albedos with the DLAM-1 model derived from Clementine imagery and absolute albedo measurements [Floberghagen *et al.*, 1999], scaled downward by a

factor of 1.3 to convert from the 750-nm Clementine imagery to an average solar wavelength (cf. Figure 7.10 of Heiken *et al.* [1991]). After accounting for the low spatial resolution of the DLAM-1 model (harmonic expansion with a wavelength of 24°), the curves are generally in good agreement, but are offset by as much as 0.03 at some longitudes.

3.2. T_7 Spectral Emissivity

[28] Having chosen T_7 as our surface temperature data set, we would like to understand the emissivity of the lunar

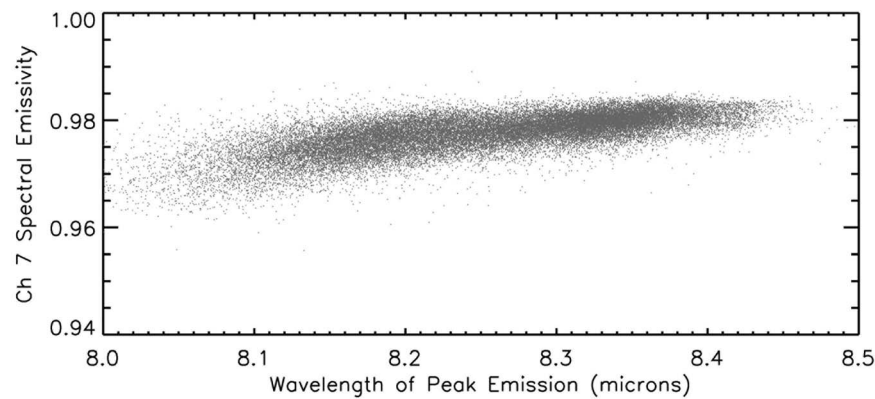


Figure 3. The wavelength of peak emission near the Christiansen Feature as derived from Diviner channel 3–5 measurements. Highlands points dominate the data below 8.28 μm , while points from maria fall at higher values.

surface in its spectral range. A decrease in ε in the mid-infrared is expected as an inherent property of lunar surface materials and a decrease in the apparent emissivity is predicted due to the anisothermality effects described above. Diviner's three narrow-band channels near 8 μm provide the ability to locate the Christiansen Feature (CF), a spectral peak in ε for particulate silicate materials [Conel, 1969]. Once it is found, the relative emissivity at other wavelengths can be calculated. We derive ε_7 relative to ε_{CF} using the method of *Greenhagen et al.* [2010] as follows.

[29] We first estimate the peak in $T_{\text{B}}(\lambda)$ corresponding to the CF by fitting a parabolic curve to $T_{3,4,5}$ to predict the wavelength of the maximum brightness temperature. The predicted brightness temperature at this wavelength is taken as the kinetic temperature of the surface, i.e., $\varepsilon_{\text{CF}} = 1$. Then ε_3 , ε_4 , and ε_5 are calculated as the ratio of the observed radiance within each bandpass to that predicted assuming blackbody emission at the kinetic temperature. We fit a parabolic curve to ε_3 , ε_4 , and ε_5 to find the magnitude and spectral location of the peak. Because our initial guess of maximum T_{B} had some error, the magnitude of the derived emissivity peak is not exactly equal to unity. We re-normalize the derived Diviner channel emissivities to the derived peak (a small correction) and adjust the derived surface temperature. Finally, ε_7 is computed as the ratio of its radiance to that of a blackbody at the derived surface temperature. We only use $T_{3,4,5}$ measurements above 250 K to avoid large solar incidence angles and to maintain high signal-to-noise ratios. These channels are not sensitive to nighttime temperatures.

[30] Because Diviner's different channels are spatially separated in the focal plane, they do not precisely overlap on the lunar surface. We therefore divide the EDS into $0.05^\circ \times 0.05^\circ$ bins each mapping cycle. We remove points with local times outside of 1000 to 1400 h to avoid large solar incidence angles and anisothermality. We reduce scatter due to slope-driven emission and insolation effects by removing points that have either local slopes $>5^\circ$ or local solar incidence angles that differ by more than 3° from that of a flat surface. The resulting bins have up to ~ 100 samples per channel, all acquired on the same LRO orbit. Radiance values in bins with at least ten samples are averaged and converted to T_{B} using the known channel spectral responses

[Paige et al., 2010a]. The emissivity calculations are performed on the averaged values of these bins.

[31] Figure 2d shows a profile of ε_7 versus longitude, smoothed by a running average of all data within 3° of longitude, every 0.05° of longitude. While there is scatter in the data, especially over the highlands, ε_7 everywhere is close to 0.98. Figure 3 shows ε_7 plotted against the location of the peak emission near 8 μm . As in the work of *Greenhagen et al.* [2010], values fall in the range between 8.1 and 8.4 μm . There is a slight trend toward higher ε_7 with increasing peak emission wavelength. The distributions with respect to both longitude and peak emission wavelength show that ε_7 is ~ 0.005 lower over the highlands than the maria. We take 0.98 as a representative value for ε_7 at all longitudes. This value is the apparent spectral emissivity at T_7 relative to the CF wavelength, when both are viewed at nadir. The same procedures were used to derive ε_6 for comparison. The trends are similar but show a stronger dependence on longitude and peak emission wavelength (and therefore composition, presumably). The means of ε_6 over the lunar highlands and maria are approximately 0.98 and 0.99, respectively.

4. Comparison of Diviner Data with Previous Model Results

[32] The primary goal of this study is to better constrain the thermophysical properties of the lunar regolith by comparing observed brightness temperatures with model predictions. This section describes our first attempt at this comparison, with refinement in section 5.

4.1. Lunar Thermal Model

[33] We use a numerical one-dimensional thermal model to predict near-surface temperatures as a function of a variety of parameters, including latitude, albedo, emissivity, planetary heat flux, and the bulk density, heat capacity, and thermal conductivity of the regolith. For lunar thermal models to accurately reproduce observed diurnal temperature curves, regolith thermophysical properties must be allowed to vary with both depth and temperature. The observed rapid cooling of the lunar surface at sunset, followed by slower cooling during the night, can be reproduced

only by models with a highly insulating upper layer (a few cm thick) overlying a lower, more conductive layer [e.g., *Keihm and Langseth*, 1973]. Furthermore, an increase in mean temperature with depth is required to fit radio observations and Apollo borehole measurements [*Linsky*, 1966; *Keihm and Langseth*, 1973; *Mitchell and de Pater*, 1994]. This characteristic is reproduced by a nonlinear dependence of the thermal conductivity on temperature. The physical explanation is that thermal radiation between grains, which is proportional to T^3 , dominates over solid conduction (within and between grains) in the upper layer at higher temperatures [*Watson*, 1964]. Solid conduction dominates in the lower layer, due to lower temperatures and perhaps more dense packing of grains.

[34] The TWO (two-layer) model described by *Vasavada et al.* [1999], validated against Apollo-era lunar measurements, laboratory data, and observations of Mercury, has the above characteristics. It models the regolith as two discrete layers, with an abrupt increase at 2-cm depth in bulk density (from 1300 to 1800 kg/m³) and in temperature-dependent thermal conductivity (from 0.0011 to 0.0094 W/m/K, at 200 K). With the following modifications, it serves as an initial basis of comparison with the Diviner data. We use a total solar irradiance at 1 AU of 1360.8 W/m², appropriate for solar minimum conditions [*Kopp and Lean*, 2011]. The geothermal heat flux is taken to be 0.016 W/m² [*Langseth et al.*, 1976; *Grott et al.*, 2010]. The model tracks lunar and solar geometries from the NAIF ephemerides over the two years of Diviner's measurements, because the influences of the Sun-Moon distance and solar declination on surface temperature, while minor, are clearly resolved by Diviner measurements.

[35] We create a look-up table of model results by running cases at the equator every 60° of longitude (because insolation is slightly longitude-dependent as orbital parameters change during the Moon's slow rotation), at ten albedos between 0.04 and 0.22, and with an emissivity of 0.98 (taken from section 3.2 but applied as a bolometric and non-directional emissivity). Each case is run for several years to allow the deepest model layers to equilibrate, and then predicted surface temperatures are output over the time span of the Diviner data used in this study. The Diviner measurements used here come from ±0.2° latitude but are modeled only at the equator, with negligible error.

4.2. Diviner T_7 Observations

[36] The model results are compared with T_7 measurements in the EDS after removing points that have either local slopes >5° or local solar incidence angles that differ by more than 3° from that of a neighboring flat surface. We use data only from the middle detector (number 11) to reduce the size of the filtered data set to 513,758 samples. Each Diviner temperature point is paired with an albedo based on its longitude, as derived in section 3. The albedo, longitude, Julian date, and local time of the measurement are used to extract the appropriate model prediction from the look-up table using bilinear interpolation.

4.3. Comparison of Diviner and Model Temperatures

[37] Figure 4a compares the filtered T_7 measurements with model predictions. Figure 4b reveals that the maria are slightly warmer than the highlands during the day, as

expected given their lower albedo. The daytime highlands temperatures contain significantly more scatter due to their greater topographic variability. This scatter reveals the limits of the existing LOLA digital elevation model for filtering out topographic effects. Inaccuracies in slope and/or slope orientations will be magnified at larger solar incidence angles and shadowing certainly plays a role (and is not accounted for in our model). Before sunrise and after sunset there are significant numbers of outlying points due to shadowing. During the night, the maria points contain more scatter than the highlands points. Topographic effects are minimized at night, but the effects of rocks are enhanced. A small subset of Diviner footprints on the maria contain a substantial fraction of warm, rocky material, resulting in measurements biased upward by tens of Kelvin [*Bandfield et al.*, 2011]. The periodic nature of the scatter, i.e., every ~2 h during the night, is an artifact of the same longitudinal segments of maria being sampled multiple times.

[38] Two conclusions are immediately apparent. The comparison validates the stratified regolith model of *Vasavada et al.* [1999] and others: the observed nighttime cooling profile is within 5 K of predictions throughout the night (Figure 4c). Homogeneous regolith models would have much larger offsets in the cooling rate during the night (cf. Figure 2 of *Vasavada et al.* [1999]). Second, excluding the minority of points affected by elevated rock abundances (see below), the highlands and maria are practically indistinguishable in their behavior at night (Figure 4b), when any differences in near-surface thermophysical properties would manifest themselves as differences in absolute temperature and/or rate of cooling.

[39] There are a few notable discrepancies (Figures 4c and 4d). Model peak daytime temperatures are lower than observed by 5–10 K. Model temperatures during the mid-to-late afternoon and early to-mid morning are up to 25 K warmer than observed on average, with the largest offsets occurring near sunrise and sunset. Model temperatures fall slightly more rapidly than observed just after sunset, but slightly less rapidly than observed during the remainder of the night. In order to quantify these discrepancies, we calculate the moving average of all model-measurement differences within 8 min, every 4 min (based on a lunar 24-h diurnal cycle). The average is calculated twice: first with all points and then excluding points outside of one standard deviation from the first mean. This curve (Figure 4d) of averaged point-by-point measurement-model offsets is an ideal way of comparing the model results with observations, since it accounts for the different albedo and orbital/celestial geometry of each point.

5. Revising Our Model of the Near-Surface Lunar Regolith

5.1. Sensitivity Studies

[40] The unprecedented accuracy and coverage of the Diviner surface temperature data allow a detailed comparison with model predictions and reveal shortcomings in our previous model assumptions, which reflect the pre-Diviner state of knowledge of the lunar surface. In this section we attempt to improve our model, with the ultimate goal of better constraining the radiative and thermophysical properties of the near-surface layer. The Moon's highly

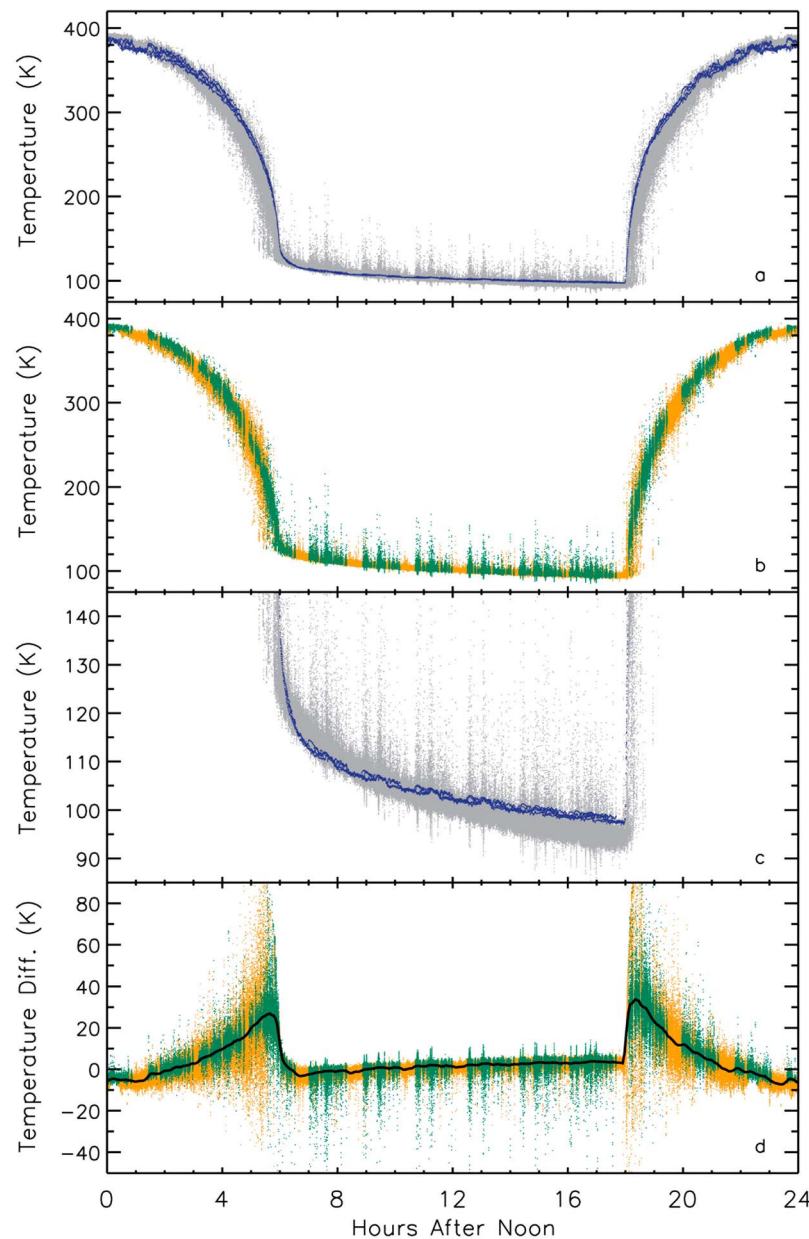


Figure 4. Initial comparison between measured and modeled equatorial surface temperature versus local time. (a) Filtered T_7 measurements (gray dots) along with corresponding point-by-point model predictions (blue). Measurements at a given local time have a range of associated albedo and orbital parameter values (and other uncertainties and errors), resulting in a spread in both the measured and modeled temperatures. (b) T_7 measurements on surfaces with Diviner albedo >0.13 (orange) and <0.09 (green), meant to roughly separate highlands and maria, respectively. (c) Same as Figure 4a, but focusing in on nighttime temperatures. (d) Difference between each model prediction and measurement, colored as in Figure 4c. The solid black line is the mean value of this difference.

insulating surface and slow rotation allow daytime temperatures to nearly equilibrate with the solar flux. Therefore daytime temperatures are influenced by topographic effects and radiative properties, but do not reveal much about bulk thermophysical properties. The offset in daytime temperatures in Figure 4d, especially those near sunrise and sunset, provide the means for adjusting the model's radiative assumptions. Nighttime temperatures, however, are diagnostic of near-surface thermophysical properties. At night

the surface radiates to space the energy stored in the regolith during the day. Because the near-surface regolith is highly insulating, heat exchange occurs only within the upper ~ 30 cm at the equator [Vasavada *et al.*, 1999], and diffusion of energy is slow. Energy from progressively deeper levels is conducted toward the surface as the night progresses. Variations in thermophysical properties with depth will manifest themselves as variations in rate of energy radiated at the surface (i.e., changes in the slope of temperature versus

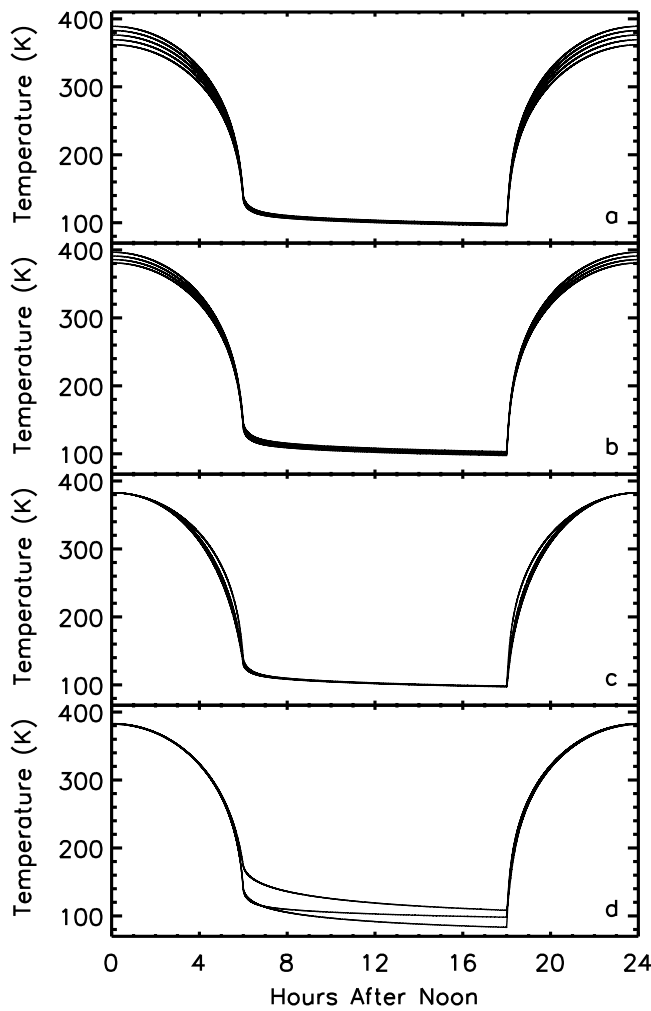


Figure 5. Sensitivity of equatorial surface temperatures to variations in thermophysical parameters. (a) Results for albedos of 0.04, 0.10, 0.16, 0.22, and 0.28, from top to bottom at noon. (b) Results for emissivities of 0.85, 0.90, 0.95, and 1.0, from top to bottom at noon. (c) Results when albedo is dependent on solar incidence angle. The top curve is for model TWO with no dependence. The next curves use $a = 0.03$ and 0.05, respectively, as described in the text. (d) Results for models BOT, TWO, and TOP from top to bottom at midnight.

time). Accordingly, Figure 4d suggests that we re-examine the precise structure of our model.

[41] We used the thermal model to conduct a set of sensitivity studies for insight into how to adjust our regolith model to better match the Diviner measurements. Figures 5a and 5b reveal how diurnal surface temperatures change over ranges of A (0.04 to 0.28) and ϵ (0.85 to 1.0) relevant for the Moon. Figure 5c shows the effect of A when dependent on solar incidence angle as described by Keihm [1984]. Figure 5d shows the effect of modest changes in bulk thermophysical properties using the TWO model along with runs where the entire surface has the properties of the upper (TOP) or lower (BOT) layer of TWO. One can see that different thermophysical parameters have separable effects on daytime and nighttime temperatures: we can adjust A and

$A(\theta)$ primarily to fit daytime temperatures. Likewise, the bulk properties (e.g., $\rho(z)$ and $k(z, T)$) can be tuned primarily to match nighttime temperatures. Large changes in bulk properties, e.g., to rock-like values, would affect daytime temperatures. But such changes would be two orders of magnitude larger than required to remove the mean nighttime offset in Figure 4d.

[42] The TWO model has an abrupt increase in thermal conductivity and density at 2-cm depth. While a variety of evidence indicates that the lunar regolith is graded or stratified in the upper few cm, the precise depth and sharpness of the transition are poorly constrained. Figure 6 shows how the characteristics of the near-surface layer affect the temperature and cooling rate during the night. An increase in thermal conductivity (while removing its temperature dependence and holding all other parameters at TOP values) has the effect of raising nighttime temperatures nearly uniformly at all times (Figure 6a). Increasing the depth at which the sharp transition in model TWO occurs creates a family of cooling profiles that share the characteristic sharp drop followed by slow cooling, but the slope change occurs at

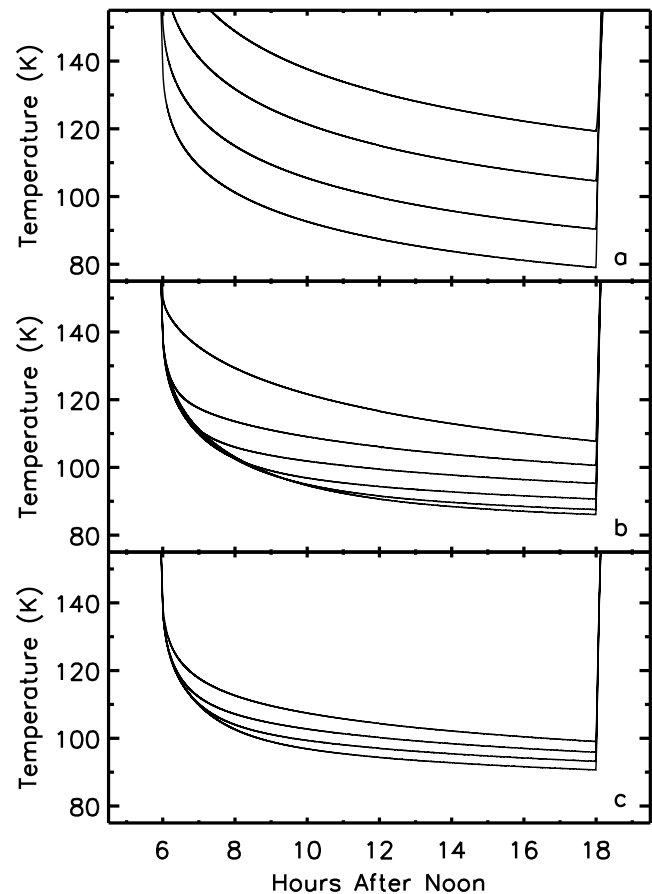


Figure 6. Sensitivity of equatorial nighttime surface temperatures to variations in thermophysical properties. (a) Results for thermal conductivities of 0.03, 0.01, 0.003, and 0.001 W/m/K, from top to bottom. (b) Results for TWO-like models where the change in properties occurs at 0.5, 1.5, 2.5, 3.5, 4.5, and 5.5 cm, from top to bottom. (c) Results for TWO-like models where the change in properties is centered at 3.5 cm but transitions linearly over 6, 4, 2, and 0 cm.

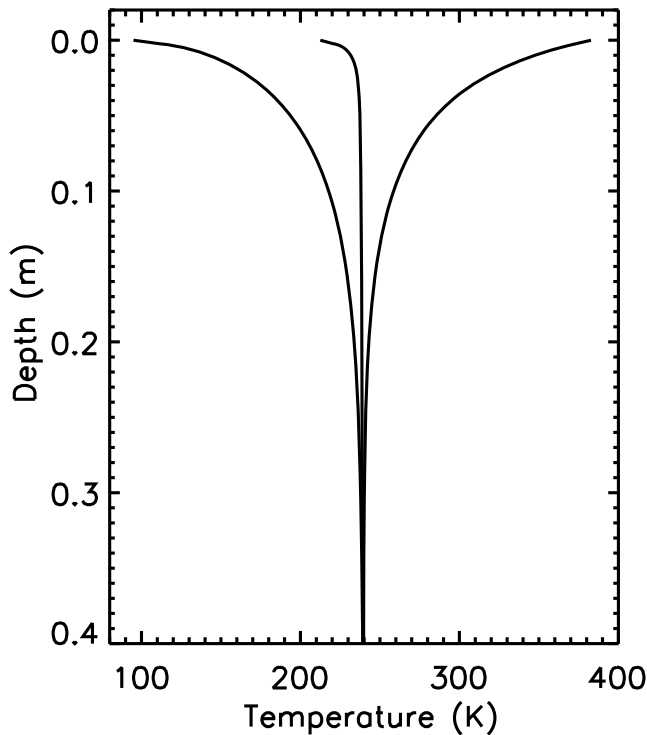


Figure 7. Depth profiles of minimum (left curve), average (center), and maximum (right) temperature for the revised model at the equator assuming a normal albedo of 0.1.

progressively later times during the night (Figure 6b). Allowing the transition to occur gradually over a depth interval has the effect of smoothing out the change in slope. This effect is difficult to isolate because such a change also affects overall temperature levels. Figure 6c shows a family of curves that change slope early in the night. But as the depth span of the transition increases, so does the time span of the change in slope. In both Figures 6b and 6c, the families of curves become parallel late in the night, when the cooling wave has penetrated deeper than the transition and is controlled by the properties at depth.

5.2. Selecting Best Fit Model Parameters

[43] We can now adjust our model parameters by comparing the details of model-measurement discrepancies in Figure 4d with the sensitivity studies in Figures 5 and 6. At the outset, we note that acceptable corrections might be found in multiple regions of parameter space (i.e., the solutions are non-unique). We use some judgment on what “knobs” to turn based on the range of values for each parameter that are consistent with the suite of existing remote, in situ, and laboratory measurements. Some parameters are left unchanged (e.g., bulk heat capacity versus T) to reduce the degrees of freedom.

[44] The adjustment to fix mid-morning and mid-afternoon model temperatures is straightforward, requiring the use of an A that depends on solar incidence angle. Because the Diviner solar reflectance data used in section 3.1 are measured normal to the surface, they cannot be used to define the full bidirectional reflectance of the surface. But daytime temperatures, being close to radiative equilibrium

with the instantaneous insolation, can be used to infer the angular dependence of albedo. We find that the Apollo-derived formulation of Keihm [1984] reproduces the observations well, where

$$A(\theta) = A_0 + a(\theta/45)^3 + b(\theta/90)^8, \quad (1)$$

and A_0 is our Diviner normal albedo at each longitude. We derive a best fit value of $a = 0.045$ (modified from 0.03) and keep Keihm’s value of $b = 0.14$.

[45] Figure 4d indicates the need for a slower thermal response relative to the initial model earlier in the night (correlated with the properties of the upper few cm) and a faster thermal response later in the night (correlated with deeper levels). Increasing the rate of cooling during the night is accomplished by changing the increase in ρ and k in the upper few cm from abrupt to gradual. We find that an exponential increase in ρ and k from a surface value to a deep bounding value produces a close fit to the cooling rate, when using an e -folding scale of 6 cm. We choose an exponential form for mathematical simplicity; fits using parabolic or other functions may fit equally well.

[46] The next step is to determine the magnitudes of ρ and k such that overall temperature values match the measurements. Several factors inform how we choose these values. Because we cannot uniquely separate the effects of ρ and k , we choose to maintain the bounds for ρ from our previous model. However, because ρ and k likely are physically related (e.g., solid thermal conductivity increases for more closely packed particles), we have them both follow the same exponential gradient with depth. Another complication is that at equatorial near-surface temperatures, k has both solid and radiative components. The nonlinear temperature dependence of the latter is responsible for the increase in mean temperature with depth observed in the Apollo

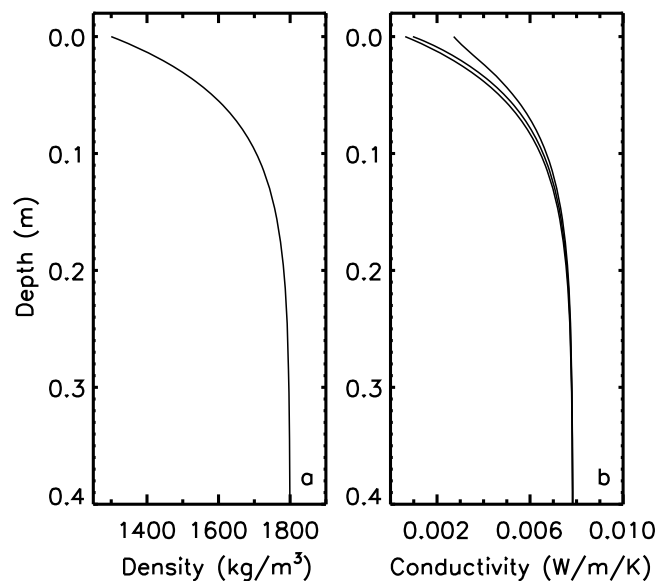


Figure 8. Depth profiles of (a) bulk density and (b) thermal conductivity in the revised model. Thermal conductivity is calculated at the minimum (left curve), average (center), and maximum (right) temperatures at each depth corresponding to Figure 7.

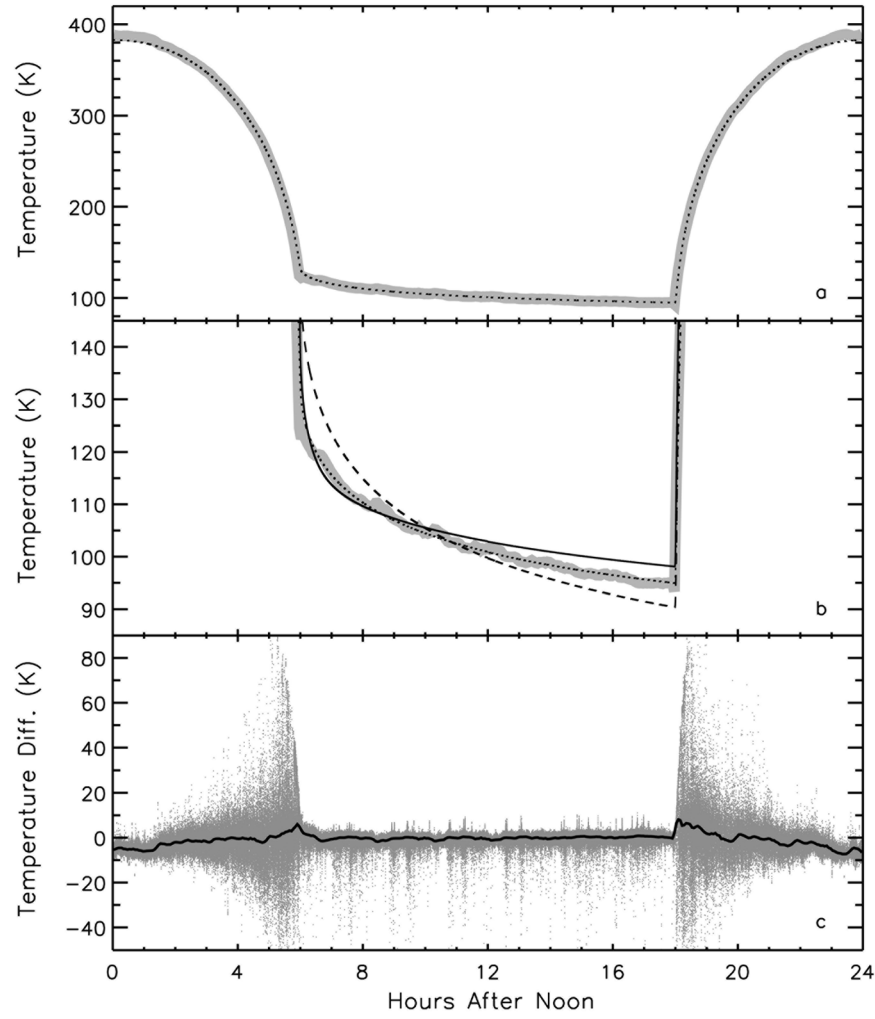


Figure 9. Revised thermal model versus Diviner measurements. (a) The thick curve is output from the TWO model, “corrected” to match the Diviner data by subtracting the model-measurement difference curve shown in Figure 4d. The dotted line is output from the revised model. (b) Same as Figure 9a, but focusing in on nighttime temperatures. The thin solid line is the TWO model, without correction (i.e., the initial model). The dashed line is a homogeneous model with a thermal conductivity of 0.003 W/m/K. (c) Difference between each measurement and its prediction from the revised model, comparable with Figure 4d. The solid black line is the mean value of this difference.

borehole measurements. This effect is often quantified as χ , the ratio of the radiative to solid component of k at $T = 350$ K. To address a deficiency in our previous model in matching the Apollo data, we increase χ to 2.7 (from 1.5) at the surface in the revised model, following *Keihm* [1984]. With these degrees of freedom eliminated, we find the best fit bounding values of k .

[47] Our formulation for ρ is

$$\rho(z) = \rho_d - (\rho_d - \rho_s) \times \exp(-z/0.06), \quad (2)$$

where the surface value is $\rho_s = 1300$ kg/m³ and the deep bound is $\rho_d = 1800$ kg/m³. The formulation for k is

$$k(z, T) = k_d - (k_d - k_s) \times \exp(-z/0.06) + \chi k_s \times (T/350)^3, \quad (3)$$

where k_s and k_d are 0.0006 and 0.007 W/m/K, respectively, and χ is 2.7. Profiles of the minimum, average, and maximum temperatures experienced at each depth using the revised model are plotted in Figure 7. The revised model ρ and k as functions of depth and modeled temperature are shown in Figure 8.

[48] The improved fit of this model to the Diviner measurements is demonstrated in Figure 9. The quantitative improvement is best seen by comparing Figures 4d and 9c, the point-by-point differences between the model predictions and the Diviner data. Nighttime offsets in magnitude and slope have been nearly eliminated, and daytime offsets are significantly reduced. In order to compare the model fits in a more physically intuitive way, we can use the initial set of model-measurement offsets (in Figure 4d) to compute a “corrected” temperature curve, by adding the offsets to the

initial TWO model, run at an arbitrary solar declination, longitude, and albedo (0° , 0° , and 0.1, respectively). Figures 9a and 9b show this ideal curve along with the results from the revised model, run with the same parameters. The revised model achieves the desired changes in magnitude and slope of nighttime temperature. Figure 9b also compares the ideal and revised curves with the results from a model with a thermal conductivity that is constant with depth and adjusted to match the Diviner data. This comparison shows that, even though the observed slope of nighttime temperatures is not as shallow as in the original TWO model, a homogenous model cannot reproduce the shape of the Diviner profile, especially in the hours just after sunset.

6. Summary

6.1. Discussion

[49] The thermophysical homogeneity of the Moon revealed by Diviner measurements along the equator (and by extension, globally) is remarkable, though not unexplained. Ubiquitous mechanical breakdown of surface materials by micrometeoroids is the dominant surface geologic process, and the resulting particulate nature of the regolith dominates over compositional differences in determining its thermal response. A small percentage of the surface exposes high thermal inertia material, including blocks, lava flows, and bedrock not yet pulverized by impactors. *Bandfield et al.* [2011] identified small regions of lower thermal inertia as well, correlated with recent \sim km-scale impacts. In our present work, these atypical surfaces are statistically insignificant and we are able to characterize the entire equatorial near-surface layer with a single set of average thermophysical properties.

[50] The Diviner measurements build on Apollo-era studies by confirming certain characteristics of the near-surface layer inferred at specific landing sites (and in returned samples). The increase in density and conductivity in the upper few cm of the regolith is a ubiquitous feature, as is the more gradual scale of the transition than inferred by some lunar studies. While our previous model had a step-wise regolith structure similar to that derived from Apollo 17 measurements [*Keihm and Langseth*, 1973], the present work indicates that the graded structure derived from Apollo 15 measurements [*Keihm et al.*, 1973] is more representative of widespread regions of the lunar surface. We derive an e -folding scale of 6 cm for the increase. While this indicates that changes in regolith properties occur below (e.g., Figure 8) the 2-cm transition in our initial model, it remains compatible with the in situ thermal diffusivity measurements of *Langseth et al.* [1976] at the Apollo 15 and 17 sites. They find thermal diffusivity to be nearly constant from \sim 10 cm to \sim 2 m depth, with greater confidence at deeper levels.

6.2. Uncertainties and Future Work

6.2.1. Albedo and Emissivity

[51] We have derived Diviner profiles of A and ε versus longitude at the equator with sufficient accuracy to remove most of the data-model discrepancies, but with significant approximations. For example, we derived a normal albedo by empirically removing the dependence of surface reflectance on phase angle from nadir measurements of reflectance over a limited range of incidence and phase angles. Lacking

a full description of the bidirectional reflectance from Diviner, we initially used the result as Lambert albedos. But in our revised model, we applied a photometric function, $A(\theta)$, found to improve the fit to daytime temperatures. As the Diviner reflectance and thermal measurements indicate, the lunar albedo depends on both the illumination and viewing geometries (and roughness/topography), and further work will characterize these dependencies.

[52] We derived ε_7 by assuming that Diviner's 8- μ m channels reveal the kinetic temperature of the surface. More accurately, ε_7 is the ratio of ε near T_7 to that at the CF, when observed at nadir. Several sources of uncertainty remain. For example, ε_{CF} may not be unity. Also, we use ε_7 in our thermal model as representative of all infrared wavelengths (and therefore also independent of temperature). Further, we assume emission is isotropic. Future work can better characterize the behavior of ε with wavelength, and with emission and viewing geometries.

[53] It is clear from the Diviner EDS data that the assumption of isotropic emission is incorrect. Noon surface temperatures measured near 8 μ m are greater than radiative equilibrium temperatures, even if one assumes that $A = 0$. At the closest Moon-Sun distance, maximum temperatures of 397.5 K and 390 K are predicted for $A = 0$ and $A = 0.07$ (mare), respectively, while the warmest measured brightness temperatures reach 399 K. The ratio of observed to expected emission is \sim 1.09 (mare). A likely explanation is that the emission has an angular distribution weighted toward the low emission angles that Diviner observes. Diviner has acquired off-nadir data to help illuminate this phenomenon. While these data are not yet fully reduced, an initial look shows that emission is indeed peaked toward low emission angles. If present, this directional distribution of emission could be an inherent property of the lunar surface material, and therefore affect its kinetic temperature, or could be an observational effect created by anisothermality and/or macroscopic roughness, for example.

6.2.2. Thermophysical Modeling

[54] Given the uncertainties remaining in the reflectance and radiance measurements and their interpretation, and the several degrees of freedom in fitting models to the data, it is expected that our understanding of the structure and properties of the near-surface regolith layer will continue to be refined. The qualitative changes derived through our analysis likely are robust. But precise values of radiative and thermophysical parameters may evolve as uncertainties decrease with additional Diviner analyses, or through independent derivations of properties from other spacecraft or laboratory experiments. In particular, Diviner observations during lunar eclipses will reveal very near-surface properties. Diviner thermal studies at different latitudes may better quantify the partitioning of thermal conductivity between the radiative and solid components. The radiative component, which increases the total conductivity by factors of a few at the equator during the day, would be much less significant at colder latitudes. Deriving the total conductivity at different latitudes will help constrain the value of χ , one of the less certain "knobs" in the present work.

[55] **Acknowledgments.** Two reviewers provided valuable suggestions for improving the manuscript. Part of this research was carried out at the Jet Propulsion Laboratory, California Institute of Technology, under a contract with the National Aeronautics and Space Administration.

References

- Bandfield, J. L., R. R. Ghent, A. R. Vasavada, D. A. Paige, S. J. Lawrence, and M. S. Robinson (2011), Lunar surface rock abundance and regolith fines temperatures derived from LRO Diviner Radiometer data, *J. Geophys. Res.*, **116**, E00H02, doi:10.1029/2011JE003866.
- Conel, J. E. (1969), Infrared emissivities of silicates: Experimental results and a cloudy atmosphere model of spectral emission from condensed particulate mediums, *J. Geophys. Res.*, **74**, 1614–1634, doi:10.1029/JB074i006p01614.
- Floberghagen, R., P. Visser, and F. Weischede (1999), Lunar albedo force modeling and its effect on low lunar orbit and gravity field determination, *Adv. Space Res.*, **23**(4), 733–738, doi:10.1016/S0273-1177(99)00155-6.
- Greenhagen, B. T., et al. (2010), Global silicate mineralogy of the Moon from the Diviner Lunar Radiometer, *Science*, **329**, 1507–1509, doi:10.1126/science.1192196.
- Grott, M., J. Knollenberg, and C. Krause (2010), Apollo lunar heat flow experiment revisited: A critical reassessment of the in situ thermal conductivity determination, *J. Geophys. Res.*, **115**, E11005, doi:10.1029/2010JE003612.
- Heiken, G., D. Vaniman, and B. M. French (Eds.) (1991), *Lunar Sourcebook*, Cambridge Univ. Press, Cambridge, U. K.
- Keihm, S. J. (1984), Interpretation of the lunar microwave brightness temperature spectrum: Feasibility of orbital heat flow mapping, *Icarus*, **60**, 568–589, doi:10.1016/0019-1035(84)90165-9.
- Keihm, S. J., and M. G. Langseth (1973), Surface brightness temperatures at the Apollo 17 heat flow site: Thermal conductivity of the upper 15 cm of regolith, *Proc. Lunar Sci. Conf.*, **5th**, 2503–2513.
- Keihm, S. J., K. Peters, M. G. Langseth, and J. L. Chute (1973), Apollo 15 measurement of lunar surface brightness temperatures: Thermal conductivity of the upper 1½ meters of regolith, *Earth Planet. Sci. Lett.*, **19**, 337–351, doi:10.1016/0012-821X(73)90084-8.
- Kopp, G., and J. L. Lean (2011), A new, lower value of total solar irradiance: Evidence and climate significance, *Geophys. Res. Lett.*, **38**, L01706, doi:10.1029/2010GL045777.
- Langseth, M. G., S. J. Keihm, and K. Peters (1976), Revised lunar heat-flow values, *Proc. Lunar Sci. Conf.*, **7th**, 3143–3171.
- Linsky, J. (1966), Models of the lunar surface including temperature-dependent thermal properties, *Icarus*, **5**, 606–634, doi:10.1016/0019-1035(66)90075-3.
- Mitchell, D. L., and I. de Pater (1994), Microwave imaging of Mercury's thermal emission at wavelengths from 0.3 to 20.5 cm, *Icarus*, **110**, 2–32, doi:10.1006/icar.1994.1105.
- Paige, D. A., et al. (2010a), The Lunar Reconnaissance Orbiter Diviner Lunar Radiometer Experiment, *Space Sci. Rev.*, **150**, 125–160, doi:10.1007/s11214-009-9529-2.
- Paige, D. A., et al. (2010b), Diviner Lunar Radiometer observations of cold traps in the Moon's south polar region, *Science*, **330**, 479–482, doi:10.1126/science.1187726.
- Smith, D. E., et al. (2010), The Lunar Orbiter Laser Altimeter investigation on the Lunar Reconnaissance Orbiter mission, *Space Sci. Rev.*, **150**, 209–241, doi:10.1007/s11214-009-9512-y.
- Tooley, C. R., M. B. Houghton, R. S. Saylor, C. Peddie, D. F. Everett, C. L. Baker, and K. N. Safdie (2010), Lunar Reconnaissance Orbiter mission and spacecraft design, *Space Sci. Rev.*, **150**, 23–62, doi:10.1007/s11214-009-9624-4.
- Vasavada, A. R., D. A. Paige, and S. E. Wood (1999), Near-surface temperatures on Mercury and the Moon and the stability of polar ice deposits, *Icarus*, **141**, 179–193, doi:10.1006/icar.1999.6175.
- Vondrak, R., J. Keller, G. Chin, and J. Garvin (2010), Lunar Reconnaissance Orbiter (LRO): Observations for lunar exploration and science, *Space Sci. Rev.*, **150**, 7–22, doi:10.1007/s11214-010-9631-5.
- Watson, K. (1964), I. The thermal conductivity measurements of selected silicate powders in vacuum from 150°–350°K. II. An interpretation of the Moon's eclipse and lunation cooling as observed through the Earth's atmosphere from 8–14 microns, Ph.D. thesis, Div. of Geol. and Planet. Sci., California Inst. of Tech., Pasadena, Calif.
- J. L. Bandfield, Earth and Space Sciences, University of Washington, Johnson Hall 070 Box 351310, Seattle, WA 98195-1310, USA.
- B. T. Greenhagen, Jet Propulsion Laboratory, California Institute of Technology, 4800 Oak Grove Dr., M.S. 183-601, Pasadena, CA 91109, USA.
- P. O. Hayne, Geological and Planetary Sciences, California Institute of Technology, Mail Code 150-21, Pasadena, CA 91125, USA.
- D. A. Paige, M. A. Siegler, and J.-P. Williams, Earth and Space Sciences, University of California, 595 Charles Young Dr. E., Los Angeles, CA 90095, USA.
- A. R. Vasavada, Jet Propulsion Laboratory, California Institute of Technology, 4800 Oak Grove Dr., M.S. 264-640, Pasadena, CA 91109, USA. (ashwin@jpl.nasa.gov)